Dynamic Behavior and Heat Transfer Characteristics of Non-spherical Ice Crystals in High-Temperature Air Flow

ZHONG Fuhao[1], *WEI Zhen*[1], *CHEN Jiajun*[1], *MIAO Qingshuo*[1], *ZHENG Mian*[1], *HOU Yu*[1], *LIU Xiufang*[1,2*]

1. School of Energy and Power Engineering, Xi'an Jiaotong University, Xi'an 710049, P.R. China;
2. Anti/De-Icing Key Laboratory, China Aerodynamics Research and Development Center(CARDC), Mianyang 621000, P.R. China

(Received 26 March 2023; revised 13 April 2023; accepted 24 April 2023)

Abstract: This study investigates the dynamic behavior and heat transfer of ice crystals in high-temperature air flow after being ingested by an aero-engine. A numerical model under the Lagrange framework is built to simulate ice crystal motion, heat and mass transfer. Different ice crystal melting models and ice crystals with various shapes and sizes are also compared. The results show that when using the "naked" ice particle model, it takes longer to completely melt compared with the water cover model. It takes 0.04 s for a 20 μm particle to melt, but the melting rate of a "naked" ice particle is faster before 0.023 s. Under the same condition, the liquid water content of a spherical ice crystal is high, and that of a 20 μm spherical one is 49.05% at the outlet. The liquid water contents of ellipsoidal and hexagonal plate ice crystals are close, which are roughly 40% at the outlet. The smaller the size, the earlier the crystals start to melt, and the higher the liquid water content of the crystals. The liquid water content is 60.4% of a 20 μm ice crystal and only 15.5% of a 40 μm one at the outlet.

Key words: ice crystals; aero-engine; Lagrange method; heat and mass transfer; non-spherical

CLC number: V231 **Document code:** A **Article ID:** 1005-1120(2023)02-0205-11

0 Introduction

Aircraft icing problems were recognized as early as the beginning of modern flight. The first reported aircraft icing can be traced back to 1920s[1]. Researchers first discovered and studied the phenomena of supercooled water droplets icing. Related prediction and protection have also been widely applied in practice[2]. However, since 1990s, there has emerged an increasing number of accidents caused by engine thrust loss at the altitude of 6.7 km even though supercooled water droplets rarely exist there. According to the accident investigation and analysis conducted by the relevant authorities, the main cause of accidents is the adhesion and freezing of ice crystals after being ingested by the engine[3].

In recent years, intensive investigations have been conducted to resolve the problem of ice crystal icing inside engines via theoretical and numerical modelling, and experiment[4-5]. For the ice crystal melting and freezing process, Villedieu et al.[6] and Trontin et al.[7] proposed the ice crystal freezing model based on the supercooled water droplet freezing model, which divided the ice crystal melting phase transition into three processes, namely sublimation of supercooled ice crystal, ice crystal melting and evaporation of droplets after melting completed. Lou et al.[8] proposed three models of ice crystal melting, which are respectively the "naked" ice model, the water film cover model and the porous model. They compared the first two models and showed that the water film cover model had a

*Corresponding author, E-mail address: liuxiufang@mail.xjtu.edu.cn.

How to cite this article: ZHONG Fuhao, WEI Zhen, CHEN Jiajun, et al. Dynamic behavior and heat transfer characteristics of non-spherical ice crystals in high-temperature air flow[J]. Transactions of Nanjing University of Aeronautics and Astronautics, 2023, 40(2): 205-215.

http://dx.doi.org/10.16356/j.1005-1120.2023.02.009

faster melting rate. Norde[9] and Nilamdeen et al.[10] used the Euler method to simulate ice crystal freezing in airfoils and engines, considering the complex processes of ice crystal adhesion, fragmentation and erosion of ice crystals. Veres et al.[11-13] applied an engine icing computational tool to simulate the flow through a turbofan engine and assess the risk of ice accretion. They found that the ice accumulation was affected by the local wet bulb temperature, ice crystal speed and ice crystal liquid water content. Feulner et al.[14-15] used the Monte Carlo particle trajectory simulation method and studied the motion and crushing process of ice crystal particles ingested by the engine, and found that the ice crystal fragmentation mainly occurred on the low-pressure compressor blades. The internal flow field, ice crystal inertia and centrifugal effect of the compressor had great effects on the radial distribution of ice crystals. Nilamdeen et al.[16-17] extended the original supercooled water icing software and developed a mixed-phase icing calculation program for air, water droplets and ice crystals, and conducted the three-dimensional modeling on the ice crystal freezing in an engine to obtain the evolution process of ice shape on the surface of stator blades.

However, relevant research in China is still in its infancy stage. Especially, the motion, heat transfer and icing characteristics of ice crystal ingested in the turbofan engine are rarely studied. Tan[18] used the Euler method to simulate the freezing of airfoil ice crystals, used the Messinger model to obtain the ice shape, and found that freezing is easier to occur in a low-pressure environment. Bu et al.[19] and Guo et al.[20] modified the Messinger model to calculate the icing of NACA0012 airfoil under mixed-phase conditions. The results showed that liquid water content, airflow temperature and ice crystal adhesion effect have great influences on the amount and profile of icing. Jiang et al.[21] used the Lagrange method to study the motion, heat transfer and adhesion of ice crystals to the engine. They obtained ice profile of the surface area of stator. Guo et al.[22] simulated the movement and heat transfer of ice crystals in a typical large icy wind tunnel configuration based on Euler method, and clarified the thermal/force balance characteristics of medium ice crystals in large icy wind tunnels. Ma et al.[23] developed an airfoil icing model on the NNWICE platform, and analyzed the influence of ice crystal shape and flow parameters on the phase transition and adhesion of moving ice crystals.

Most of the reported studies simplify ice crystals as spherical particles. Ice crystals in clouds can undergo freezing and condensation, leading to complex shapes and size distributions. Therefore, in simulations of ice crystal freezing, it is crucial to take into account the impact of irregular particles which can affect the behavior of ice crystals. Naturally-formed ice crystals also have different melting phase transition processes under high-speed air flows, so it is necessary to compare and analyze different melting models. In this study, by using the Lagrange method, the dynamic behavior and heat and mass transfer of ice crystals after being ingested into an engine are investigated numerically. The heat transfer characteristics of ice crystals inside an aircraft engine are obtained. In the model, different melting models of crystals are compared, and the effects of shape irregularity of ice crystals and compressor blade thickness are examined. This study consolidates the foundation for further numerical simulation on ice crystal icing phenomena in aircraft engines.

1 Numerical Modeling

According to the two-phase flow theory, the icing condition of aircraft ice crystals is in the range of unidirectional coupled dilute two-phase flow, and the following assumptions are made.

(1) Only consider the effect of air flow on ice crystals, and neglect the effect of ice crystals to air flow.

(2) Ice crystals neither condense nor break in motion.

(3) Neglect internal temperature variation of an ice crystal, and the viscosity and density remain unchanged during the movement.

1.1 Motion and heat transfer model of ice crystals

In the engine flow channel, the ice crystal particles are affected by a variety of forces, including viscous force F_D, gravity and buoyancy F_G, Magnus force F_M, Basset force F_B, etc. According to Newton's second law

$$M_{ice}\frac{d\boldsymbol{u}_{ice}}{dt}=F_D+F_G+F_B+F_M \tag{1}$$

where M_{ice} is the mass of the ice crystal and $d\boldsymbol{u}_{ice}/dt$ the acceleration of the ice crystal. M_{ice} is a function of the radius of ice crystals shown as

$$M_{ice}=4\pi\rho_{ice}R_{ice}^3/3 \tag{2}$$

where ρ_{ice} is the ice density and R_{ice} the radius of ice crystals.

Since ice density is much greater than that of air, and the size of an ice crystal is small, the viscous force is two to three orders of magnitude greater than gravity, only the viscous force is considered, and other forces such as gravity with smaller magnitude are negligible. Combined with the drag coefficient, the equation of motion can be expressed as

$$\frac{d\boldsymbol{u}_{ice}}{dt}=\frac{3C_D\rho_{air}}{8\rho_{ice}R_{ice}}|\boldsymbol{u}_{air}-\boldsymbol{u}_{ice}|(\boldsymbol{u}_{air}-\boldsymbol{u}_{ice}) \tag{3}$$

where ρ_{air} is the air density, C_D the drag coefficient of ice crystals, $\boldsymbol{u}_{air}$ the airflow velocity, and $\boldsymbol{u}_{ice}$ the ice crystal velocity.

Lawson et al.[24] measured and generalized the size and shape of ice crystal particles in cirrus clouds. The classification of the ice crystal shape is shown in Fig.1(a). They are categorized into the following mathematical models: Spherical, ellipsoidal, columns, hexagonal plate ice crystals, as shown in Fig.1(b).

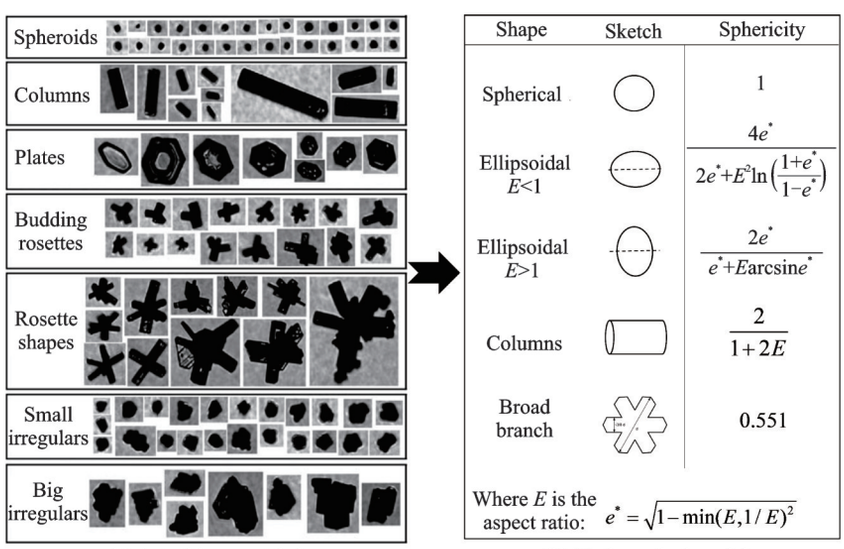

(a) Actual ice crystal shape (b) Mathematical model

Fig.1 Classification of the shape of ice crystal particles in clouds and simplifying mathematical models[24]

The sphericity is defined by $\Phi=A_p/A$, where A_p is the surface area of the sphere with the same volume as the ice crystal, and A the actual surface area of the ice crystal. Φ is used to measure the degree to which the non-spherical ice crystal approximates the spherical shape, and then further correct the drag coefficient and heat and mass transfer coefficient of the movement. By comparing the C_D correction methods of various non-spherical particles proposed in the studies[9,25-26], the empirical correlation of spherical, ellipsoidal and Columns is

$$C_D(Re,\Phi)=\frac{24}{Re}(1+A\cdot Re^B)+\frac{C}{1+D/Re} \tag{4}$$

where $A(\Phi)=\exp(2.328\,8-6.458\,1+2.448\,6\Phi^2)$; $B(\Phi)=0.096\,4+0.556\,5\Phi$; $C(\Phi)=\exp(4.905-13.894\,4\Phi+18.422\,2\Phi^2-10.259\,9\Phi^3)$; $D(\Phi)=\exp(1.468\,1+12.258\,4\Phi-20.732\,2\Phi^2+15.885\,5\Phi^3)$.

Calculation empirical correlation of C_D with a

hexagonal plate ice crystal

$$C_D = \left(\frac{64}{\pi Re}\right)(1 + 0.142Re^{0.887}) \tag{5}$$

where Re is the relative Reynolds number.

The ice crystals that are sucked into the engine experience a temperature difference with the surrounding hot air. As a result, the outer surface of the ice crystal melts into a water film, which either falls off or covers the surface of the ice crystal and continues to evaporate. Due to this melting process, the diameter of the ice crystal particles decreases. This phase change melting process can be simplified into the following two idealized models.

The first model is the "naked" ice particle model, where the ice crystal particles are always in contact with air without any external water layer. In this model, once the outer surface melts, the resulting water film is blown away from the surface of the ice particles. The second model is the water cover model, where the water film resulting from melting covers the outer surface of the ice crystal particles, as shown in Fig.2.

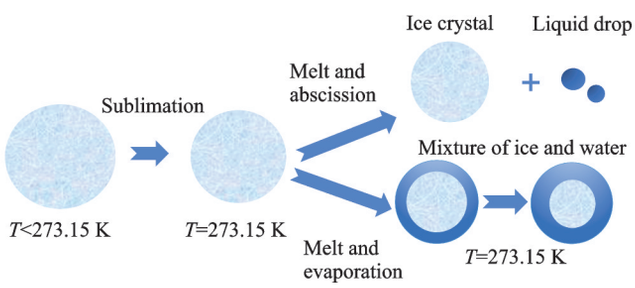

Fig.2 Schematic diagram of two melting models

The initial stage of both models involves the sublimation process of supercooled ice crystals, with a heat transfer relationship as

$$hA(T_{air} - T_{ice}) + L_{sg}\frac{dM_{ice}}{dt} = C_{pi}M_{ice}\frac{dT_{ice}}{dt} \tag{6}$$

The mass transfer relation is

$$\frac{dM_{ice}}{dt} = h_m A(\rho_{ga} - \rho_{gi}) \tag{7}$$

where h is the convective heat transfer coefficient on the surface of the ice crystal, C_{pi} the specific heat capacity of ice crystals, h_m the mass transfer coefficient on the surface of ice crystals, ρ_{ga} the density of water vapor in the air, ρ_{gi} the saturation vapor density on the surface of the ice crystal, T_{air} the airflow temperature, T_{ice} the ice temperature, and L_{sg} the sublimation heat of ice.

For the "naked" ice model, after the ice crystals begin to melt, all the heat absorbed from the air is used for the melting process, and the energy balance equation is

$$\frac{dM_{ice}}{dt} \cdot L_{sl} = hA(T_{air} - T_{ice}) \tag{8}$$

where L_{sl} is the melting heat of ice crystals.

For the water cover model, after the ice crystals begin to melt, the heat absorbed from the air is used for the melting of ice crystals and the evaporation of the water film. The energy conservation relationship therefore is

$$hA(T_{air} - T_{ice}) = L_{lg}\frac{dM_g}{dt} + L_{sl}\frac{dM_{ice}}{dt} \tag{9}$$

where L_{lg} is the heat of vaporization of water, L_{sl} the heat of melting of ice crystals, and M_g the mass of water film evaporated into vapor.

The mass of the ice-water mixture is the summation of those of ice and water, which is also equivalent to the mass of the ice-water mixture at the initial moment of melting minus the mass of evaporated water vapor

$$M_{mix} = M_{ice} + M_{water} = M_{sm} - M_g \tag{10}$$

where M_{mix} is the mass of the ice-water mixture, M_{water} the mass of water in the ice-water mixture, and M_{sm} the mass of the ice-water mixture at the initial moment of melting.

The equivalent density ρ_{mix} of ice-water mixtures can be determined by the mass of ice and wa-

ter as

$$\rho_{\mathrm{mix}}=\frac{M_{\mathrm{ice}}}{M_{\mathrm{mix}}}\rho_{\mathrm{ice}}+\frac{M_{\mathrm{water}}}{M_{\mathrm{mix}}}\rho_{\mathrm{water}} \tag{11}$$

Assuming that the water film produced after the melting of ice crystals evenly covers the surface of the particles, the equivalent radius R_{mix} of the ice-water mixture can be calculated from the equivalent density

$$R_{\mathrm{mix}}=\sqrt[3]{3M_{\mathrm{mix}}/\left(4\pi\rho_{\mathrm{mix}}\right)} \tag{12}$$

Similarly, the heat transfer of non-spherical particles is corrected, and the number of non-spherical particles Nu is calculated as[26]

$$Nu=2\sqrt{\Phi}+0.55Pr^{1/3}\Phi^{1/4}\sqrt{Re} \tag{13}$$

where Pr is the Prandtl number.

The mass transfer coefficient of ice crystal or ice-water mixture is obtained by heat and mass transfer analogy as

$$h_{\mathrm{m}}=\frac{h}{\rho_{\mathrm{air}}C_{\mathrm{pa}}Le^{2/3}} \tag{14}$$

where C_{pa} is the specific heat capacity of air, and Le the Lewis number.

The density of ice crystals is 919.1 kg/m^3 in this study, and the thermophysical parameters of water and air including density, viscosity, specific heat capacity and thermal conductivity are calculated according to temperature interpolation.

1.2 Engine flow channel model

This study uses the typical low-pressure stage compressor model of Ref. [27] for calculation. Fig. 3 shows a five-stage compressor planar blade grid, with each stage composed of rotors and stators.

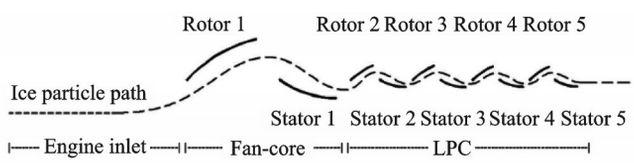

Fig.3 Schematic diagram of ice crystals passing through the interior of a low-pressure stage compressor[27]

The NACA airfoil family thickness distribution is adopted[28]. In order to facilitate the calculation, a polynomial expression is selected as

$$y=\pm\frac{c}{0.2}\left(0.296\,90\sqrt{x}-0.126\,00x-0.351\,60x^2+0.284\,30x^3+0.101\,50x^4\right) \tag{15}$$

where $c=5\%$ is the relative thickness, and x and y are dimensionless horizontal and ordinate coordinates of the blade profile line relative to the chord length, respectively.

Ref. [22] is used to perform triangulation on the inlet and outlet of the rotor. This provides the axial and circumferential velocities of airflow within the flow channel. Interpolation and calculation are then used to determine the temperature and pressure of the airflow at all stages. The calculation follows a discrete time and progressive space method, as depicted in Fig.4.

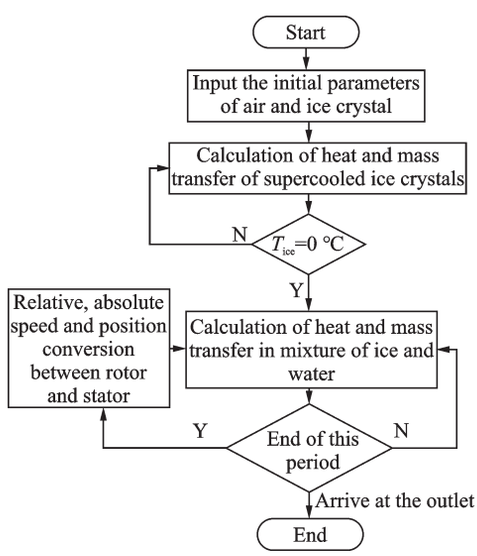

Fig.4 Calculation flow chart

2 Result Analysis

2.1 Comparison of two melting models

The "naked" ice particle model and the water-covered model are both simplified. It is neces-

sary to compare the two models as they both exist in actual processes.

In Fig.5, a comparison is made between the melting processes of the "naked" ice particle model and the water-covered model under the same high-temperature air flow environment and with the same initial conditions of ice crystals. The specific running parameters are: constant airflow environment with U_{air} =50 m/s, T_{air}=50 ℃, h=10%; R_{ice}=20 μm, T_{ice}=−20 ℃ for ice crystal initial conditions. The melting trends of the two models are similar, but the "naked" ice particle model takes longer to completely melt under the same working conditions. Specifically, the 20 μm particle takes 0.038 s to completely melt in the "naked" ice particle model. This is because, in the "naked" ice particle model, the radius of the ice crystal decreases over time, resulting in a reduction of the surrounding air convection heat transfer area. This, in turn, it leads to lower convective heat transfer during the later stages of melting compared to earlier stages. In contrast, when covered with a water film, the outside of the ice particle is wrapped with a water film, which keeps the heat exchange area and heat exchange rate essentially constant. Therefore, the melting time is shorter in the water-covered model.

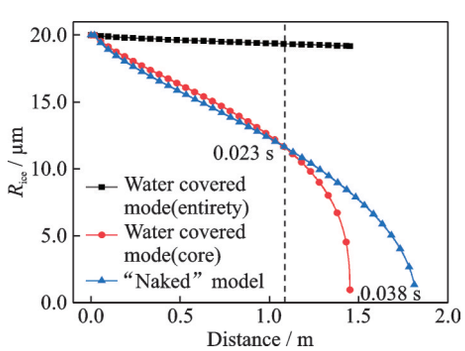

Fig.5 Comparison of melting processes in the "naked" ice particle model and the water cover model

Furthermore, it can be observed that, during the initial melting stages before 0.023 s, the "naked" ice particle model actually melts slightly faster than the water-covered model. This can be attributed to the fact that, in the water-covered model, the presence of the water film means that some of the convective heat transfer must be used to evaporate the water film. This results in less heat being available for melting the ice crystals.

Therefore, in the early stages of melting, the presence of the water film slows down the melting rate due to the energy required for evaporation. However, in the middle and late stages of melting, the water film increases the convective heat transfer area such that it is much larger than that of the anhydrous film in the "naked" ice particle model. This leads to a more significant heat exchange, thereby accelerating the melting speed. Overall, the presence of the water film covering accelerates the melting of ice crystals.

2.2 Effect of initial conditions of ice crystals on motion heat transfer

Fig.6 shows the movement of ice crystals (equivalent volume diameter is 40 μm) of different shapes inside the compressor after being sucked in from the same position. The columns ice crystals collide in turn with the third and the fourth stage stator, with a liquid water content of 15.3% when colliding with the fourth stage stator. The hexagonal plate ice crystal collides with the third stage rotor and third stage stator with the liquid water content of 12.3%.

In Fig.7, the change in liquid water content along the axial position is shown after ice crystals of different shapes, but at the same initial position, are sucked into the compressor. The percentage content of liquid water mass of different shapes of ice crystals along the axial direction gradually increases. The liquid water content of spherical ice crystals is the largest at the same position, while the liquid water content of ellipsoidal and hexagonal ice plate crystals is similar. Specifically, at the outlet of the low-pressure compressor, the liquid water content of spherical, ellipsoidal, column-shaped, and hexagonal ice plate crystals is 49.05%, 44.32%, 29.74%, and 37.13%, respectively.

Fig.8 shows the speed variation of ice crystals

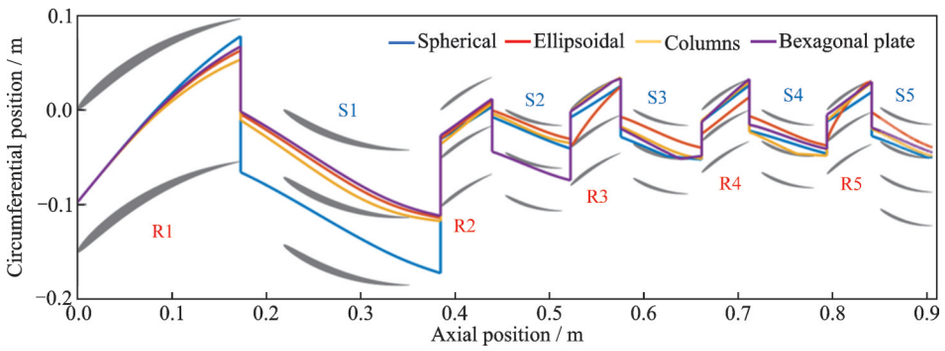

Fig.6 Trajectory of ice crystals with different shapes after inhalation

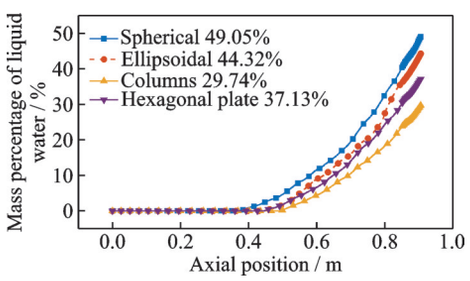

Fig.7 Changes in liquid water content after inhalation of ice crystals with different shapes

along the axial positions after different shapes of ice crystals are sucked in from the same position. The gray dotted line is the axial velocity of air, and collisions between the first stage of rotor and stator are absent before 400 mm. The ice crystals continue to accelerate in the air flow, and their final speed approaches that of air. The subsequent velocity change follows the same trend as air. The occurrence of collision can also be found in the distribution of axial velocity, such as ellipsoidal ice crystals (red curve) violently colliding at the head of the third stage rotor. This results in greatly reduced axial velocity and an almost total loss of axial momentum due to a direct impact at the front end of the fifth stage rotor.

It is evident that there is a noticeable difference

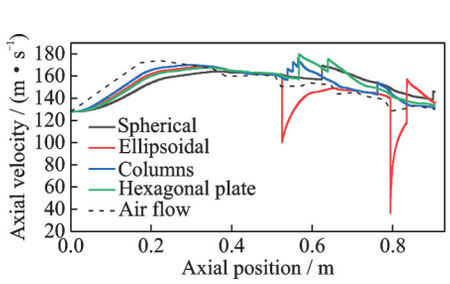

Fig.8 Changes in axial velocity of ice crystals with different shapes after suction

between spherical and non-spherical ice crystals in terms of their motion during the phase transition. Combining Figs.7 and 8, it can be found that when there is no collision effect, the speed of columnar particles increases the fastest , and that of spherical particles increases slower, because non-spherical particles have greater viscous force and greater acceleration in the air flow. Since spherical particles move more slowly in the air flow, the same axial displacement takes longer, which increases the heat and mass transferred between the hot air and the ice crystals, resulting in the maximum water content of spherical liquids and the lowest water content of columnar liquids. Due to the consistency of motion and melting laws, it can also be concluded that non-spherical characteristic indirectly affects the melting behavior through the particle trajectory and velocity in this study.

Fig.9 shows the variations in heat transfer coefficient for three ice crystal shapes in the engine runner. The heat transfer coefficient of the three ice crystal shapes are basically the same following the axial position trend with oscillatory fluctuations. The heat transfer coefficient of spherical ice crystals is large, and that of column ice crystals is small, attributed by the large difference between spherical ice crystals and air velocity. This difference not only affects the movement of ice crystals but also influences heat exchange. At an axial position of approximately 0.8 m, the ellipsoidal ice crystal had a violent collision, resulting in a significant difference between its axial velocity and air velocity, and a sudden increase in the heat transfer coefficient.

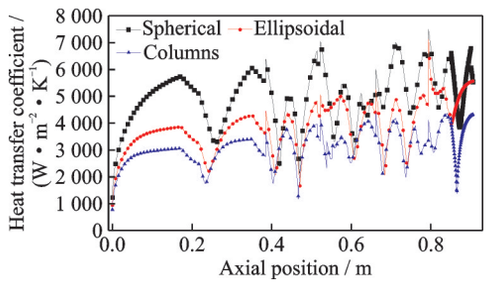

Fig.9 Changes in heat transfer coefficient after inhalation of ice crystals with different shapes

Fig.10 shows trajectories of ice crystals as they move within the compressor at various radii after being ingested. The larger the radius of the ice crystal, the stronger the inertia which results in upward drift of the trajectory. Ice crystals with a radius of 10 μm (yellow trajectory) collide with the third rotor and fourth stage stator where the liquid water content reaches 86.96%. As a result, the possibility of adhesion of 10 μm ice crystals on the fourth stage stator is greater. Ice crystals with a radius of 20 μm (purple trajectory) collide with the third stage stator, the fourth stage rotor and the fifth stage rotor. The liquid water content at the collision point is 45.53%, so the ice crystal with a radius of 20 μm is more likely to adhere to the third stator. Ice crystals with a radius of 100 μm (blue trace) collide with the first stage rotor, the first stator, and the third stage rotor, with the liquid water content still less than 10% at the outlet of the compressor. Therefore, ice crystals with a radius of 100 μm may not adhere nor freeze inside the low-pressure stage compressor.

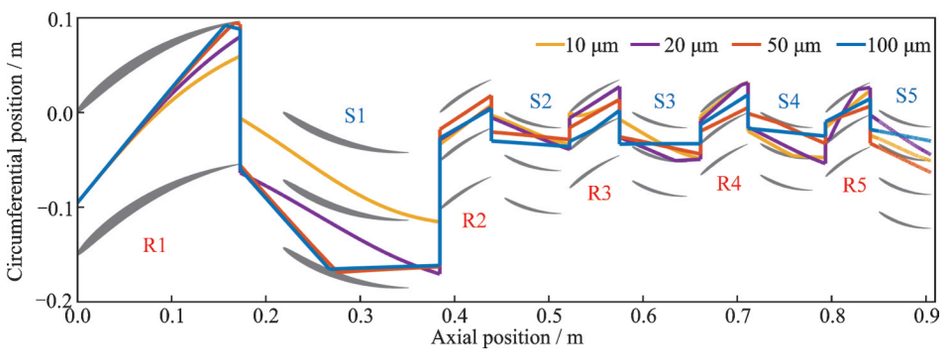

Fig.10 Trajectory of ice crystals with different radii after inhalation

Fig.11 shows the axial temperature variation inside the compressor after inhalation of ice crystals with different radii and the same initial temperature. Ice crystals are warmed up from supercooled to 0 ℃ along the axis before starting to melt. The smaller the ice crystals, the faster the temperature increases to reach 0 ℃. Ice crystals with a large size, such as those with a radius of 100 μm (purple curve), travel farther inside the compressor and enter the fifth stage of rotor and stator before they start melting. Due to their low liquid water content, the likelihood of adhesion and freezing is also low.

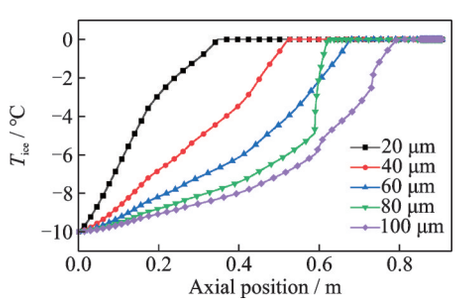

Fig.11 Temperature changes after inhalation of ice crystals with different radii

Figs.12 and 13 respectively show the melting rate and percentage variation of liquid water mass in the compressor after inhalation of ice crystals with different radii. The melting rates of ice crystals with different radii remain stable after melting starts. The liquid water content also increases slowly after melting starts. However, ice crystals with different radii begin to melt at different locations. The smaller the size, the earlier the crystals begin to melt. The melting rate for a larger size is faster, which is due to the larger surface area for heat transfer.

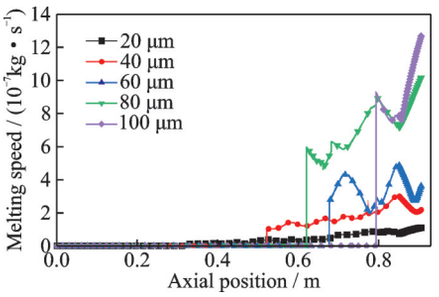

Fig.12 Melting rate of ice crystals with different radii changes after inhalation

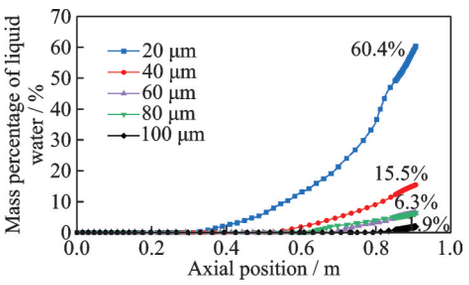

Fig.13 Percentage content of liquid water mass after inhalation of ice crystals with different radii changes

The 80 μm particles exhibit a unique behavior in the front of the third stage stator (at approximately 0.6 m), which is due to their violent collision with the front of the blade. This collision results in a great decrease in the axial velocity of ice crystals, causing its speed to be greatly different from air flow speed, thereby enhancing heat exchange. Furthermore, due to the decreased velocity, the heat transfer time is longer under the same displacement, resulting in a sudden increase in the temperature, melting speed and liquid water content of the particle. Fig.13 shows that the liquid water content of 20, 40, 60, 80, and 100 μm at the outlet of the low-pressure compressor is 60.4%, 15.5%, 6.3%, 6.3%, and 1.9%, respectively. The liquid water content of the 60 μm ice crystal is less than 10% as it reaches the outlet. Therefore, ice crystals with size greater than 60 μm are difficult to adhere and freeze in the flow channel of the low-pressure compressor.

3 Conclusions

The study utilized a numerical model under the Lagrange framework to analyze the dynamic behavior and heat and mass transfer of ice crystals in the flow channel of an aeroengine after ingestion. The main conclusions are as follows:

(1) Two melting models of ice crystal particles were compared and analyzed. The results showed that the "naked" ice particle model took longer to fully melt compared to the water-covered model. The 20 μm particle took 0.04 s to melt, while the "naked" ice particle melted faster before 0.023 s.

(2) The liquid water content of spherical ice crystals was higher compared to other shapes under the same conditions. Specifically, at the outlet, the liquid water content of 20 μm spherical ice crystals was calculated to be 60.7%. On the other hand, the liquid water content of ellipsoidal and hexagonal plate ice crystals was close, with both shapes having a liquid water content around 40% at the outlet.

(3) The initial diameter affected motion and heat transfer of ice crystals in the compressor. The smaller the size, the earlier it started to melt, and the higher the liquid water content. The 20 μm crystal's liquid water content at the outlet was as high as 60.7%, while the 40 μm one was only 17.8% under the same condition. The liquid water content at the outlet of the 60 μm ice crystal was close to 10%, enabling difficulty for the crystal to adhere to the ice.

References

[1] LEARY W M. We freeze to please: A history of NASA's icing research tunnel and the quest for flight safety[M]. [S.l.]: National Aeronautics and Space Administration, 2002.

[2] VANZANTE J F, IDE R F, STEEN L, et al. NASA glenn icing research tunnel: 2014 cloud calibration[C]//Proceedings of SAE AC-9C Aircraft Icing Technology Committee Fall 2014 Meeting. [S.l.]: SAE, 2014.

[3] JEANNE G M, WALTER S, PHILIP C. The ice particle threat to engines in flight: AIAA-2006-206[R]. Reston, VA: AIAA, 2006.

[4] HUANG Ping, BU Xueqin, LIU Yiming, et al. Mixed phase/glaciated ice accretion: Review[J]. Acta

Aeronautica et Astronautica Sinica, 2022, 43(5): 025178. (in Chinese)

[5] YUAN Qinghao, FAN Jiang, BAI Guangchen. Review of ice crystal icing in aero-engines[J]. Journal of Propulsion Technology, 2018, 39(12): 2641-2650. (in Chinese)

[6] VILLEDIEU P, TRONTIN P, CHAUVIN R. Glaciated and mixed phase ice accretion modeling using ONERA 2D icing suite[C]//Proceedings of the 6th AIAA Atmospheric and Space Environments Conference. [S.l.]: AIAA, 2014: 2199.

[7] TRONTIN P, BLANCHARD G, VILLEDIEU P. A comprehensive numerical model for mixed-phase and glaciated icing conditions[C]//Proceedings of the 8th AIAA Atmospheric and Space Environments Conference. [S.l.]: AIAA, 2016: 3742.

[8] LOU D, HAMMOND D W. Heat and mass transfer for ice particle ingestion inside aero-engine[J]. Journal of Turbomachinery, 2011, 133(3): 031020.

[9] NORDE E. Eulerian method for ice crystal icing in turbofan engines[M]. [S.l.]: University of Twente, 2017.

[10] NILAMDEEN S, HABASHI W G. FENSAP-ICE: Modeling of water droplets and ice crystals: AIAA-2009-4128[R]. [S.l.]: AIAA, 2009.

[11] VERES J P, JORGENSON P C. Modeling commercial turbofan engine icing risk with ice crystal ingestion[C]//Proceedings of the 5th AIAA Atmospheric and Space Environments Conference. [S.l.]: AIAA, 2013: 2679.

[12] VERES J P, JORGENSON P C E, JONES S M, et al. Modeling of a turbofan engine with ice crystal ingestion in the NASA propulsion system laboratory[C]//Proceedings of Turbo Expo: Power for Land, Sea, and Air. [S.l.]: American Society of Mechanical Engineers, 2017.

[13] JORGENSON P C E, VERES J P, NILI S, et al. Analysis of the honeywell uncertified research engine with ice crystal cloud ingestion at simulated altitudes[J]. Journal of Turbomachinery, 2020, 142(6): 061006.

[14] FEULNER M, LIAO S, ROSE B, et al. Ice crystal ingestion in a turbofan engine[C]//Proceedings of SAE International Conference on Icing of Aircraft, Engines, and Structures. [S.l.]: SAE, 2015.

[15] LIAO S, LIU X, FEULNER M. An analysis of turbofan inlet water and ice concentration effects in icing conditions[C]//Proceedings of SAE International Conference on Aircraft and Engine Icing and Ground Deicing. [S.l.]: SAE, 2011.

[16] NILAMDEEN S, HABASHI W, AUBÉ M, et al. FENSAP-ICE: Modeling of water droplets and ice crystals[C]//Proceedings of the 1st AIAA Atmospheric and Space Environments Conference. [S.l.]: AIAA, 2009: 4128.

[17] NILAMDEEN S, RAO V S, SWITCHENKO D, et al. Numerical simulation of ice crystal accretion inside an engine core stator[C]//Proceedings of International Conference on Icing of Aircraft, Engines, and Structures. [S.l.]: [s.n.], 2019.

[18] TAN Yan. Numerical calculation of 2D airfoil ice crystal icing based on Euler method[J]. Aeroengine, 2020, 46(4): 30-35. (in Chinese)

[19] BU Xueqin, LI Hao, HUANG Ping, et al. Numerical simulation of mixed phase icing on two-dimensional airfoil[J]. Acta Aeronautica et Astronautica Sinica, 2020, 41(12): 124085. (in Chinese)

[20] GUO Qilei, NIU Junjie, AN Bo, et al. Numerical simulation of ice crystal icing under mixed-phase conditions[J]. Acta Aerodynamica Sinica, 2021, 39(2): 168-175. (in Chinese)

[21] JIANG Feifei, DONG Wei, ZHENG Mei, et al. Phase change heat transfer characteristic of ice crystal ingested into turbofan engine[J]. Journal of Aerospace Power, 2019, 34(3): 567-575. (in Chinese)

[22] GUO Xiangdong, HU Zhanwei, DING Liang, et al. Numerical investigation of thermal and mechanical equilibrium characteristics of ice crystal in large icing wind tunnel[J]. Journal of Aerospace Power, 2022, 37(3): 478-491. (in Chinese)

[23] MA Yijian, CHAI Delin, WANG Qiang, et al. Phase change and adhesion characteristics of ice crystal movements in wing icing[J]. Acta Aeronautica et Astronautica Sinica, 2023, 44(1): 627817. (in Chinese)

[24] LAWSON R P, BAKER B, PILSON B, et al. In situ observations of the microphysical properties of wave, cirrus, and anvil clouds. Part Ⅱ: Cirrus clouds[J]. Journal of the Atmospheric Sciences, 2006, 63(12): 3186-3203.

[25] MARSHALL W R, RANZ W E. Evaporation from drops—Part Ⅰ[J]. Chemical Engineering Progress, 1952, 48(3): 141-146.

[26] VEILLARD X, ALIAGA C, HABASHI W G. FENSAP-ICE modeling of the ice particle threat to engines in flight[C]//Proceedings of SAE Aircraft & Engine Icing International Conference. [S.l.]: SAE, 2007.

[27] JOSEPH P V, PHILIP C E, RYAN C. Modeling of commercial turbofan engine with ice crystal ingestion; follow-on: AIAA-2014-2899[R]. Reston, VA: AIAA, 2014.

[28] ZHANG Xinyi. Optimization design of high load compressor blade based on curvature control[D]. Shanghai: Shanghai Jiao Tong University, 2020. (in Chinese)

Acknowledgements This work was supported by the Key Laboratory of Icing and Anti/De-icing of CARDC (No. IADL 20220107), the National Science and Technology Major Special Funds of China (No. J2019-Ⅲ-0010-0054), and the National Natural Science Foundation of China (No. 52076164).

Authors Mr. **ZHONG Fuhao** received the B.S. degree in Energy and Power Engineering from Xi'an Jiaotong University in 2022. His research interests include ice crystal icing numerical computation, and experimental technology for heat transfer in thin water film, etc.

Dr. **LIU Xiufang** received the Ph.D. degree in Power Engineering and Engineering Thermophysics from Xi'an Jiaotong University in 2013. She is currently an associate professor in School of Energy and Power Engineering, Xi'an Jiaotong University, Shaanxi, China. Her research interests include refrigeration and cryogenic technology in aerospace and thermal management technology, etc.

Author contributions Dr. **LIU Xiufang** designed the study and conducted the analysis. Prof. **HOU Yu** provided suggestions for the theoretical part and structure of the manuscript. Mr. **ZHONG Fuhao** interpreted the results and wrote the manuscript. Mr. **CHEN Jiajun** contributed to data for the analysis of the manuscript. Mr. **MIAO Qingshuo**, Mr. **WEI Zhen** and Ms. **ZHENG Mian** contributed to the discussion and background of the study. All authors commented on the manuscript draft and approved the submission.

Competing interests The authors declare no competing interests.

(Production Editor: WANG Jing)

热气流环境下非球形冰晶的运动换热特性

钟富豪[1], 魏 震[1], 陈佳军[1], 苗庆硕[1], 郑 勉[1], 侯 予[1], 刘秀芳[1,2]

(1.西安交通大学能源与动力工程学院,西安 710049,中国;
2.中国空气动力研究与发展中心结冰与防除冰重点实验室,绵阳 621000,中国)

摘要:针对冰晶被航空发动机吸入后在热气流环境下的运动换热问题,建立了拉格朗日框架下冰晶运动-传热传质耦合的数值计算方法,对比了不同的冰晶融化模型和不同形状、粒径冰晶的运动换热差异。结果表明,相较于水覆盖模型,使用"裸"冰粒子模型时完全融化需要更长时间,20 μm粒子需要0.04 s才能完全融化,但0.023 s之前"裸"冰粒子的融化速率却更快;相同条件下球形冰晶液态水含量较高,20 μm球形冰晶在计算出口处液态水含量为49.05%。椭球形和宽六角形冰晶液态水含量很相近,出口处液态水含量为40%左右;粒径越小,越早开始融化,冰晶液态水含量总是更高。20 μm的冰晶在出口处液态水含量高达60.4%,而40 μm冰晶在出口处液态水含量只有15.5%。

关键词:冰晶;航空发动机;拉格朗日法;传热传质;非球形